High Efficiency NIR Luminescence Beyond 900 nm Through Promoting Cr^{3+} Pair Generation in $Sr_3Zr_2O_7$ Layered Perovskite

Zhiyuan Pan[a], Sihan Feng[a], Yun Wang[a], Xuejiao Wang[b,*], Qi Zhu[a], Ji-Guang Li[c,*]

[a] *Key Laboratory for Anisotropy and Texture of Materials (Ministry of Education), School of Materials Science and Engineering, Northeastern University, Shenyang, Liaoning 110819, China*

[b] *School of Materials and Environmental Engineering, Bohai University, Jinzhou, Liaoning 121007, China*

[c] *Research Center for Electronic and Optical Materials, National Institute for Materials Science, Tsukuba, Ibaraki 305-0044, Japan*

[*]Corresponding author
Dr. Xuejiao Wang
Bohai University
Tel: +86-416-3400708
E-mail: wangxuejiao@bhu.edu.cn

Dr. Ji-Guang Li
National Institute for Materials Science
Tel: +81-29-860-4394
E-mail: li.jiguang@nims.go.jp

Abstract

The near-infrared (NIR) light of 900-1100 nm exhibits enormous application potential in fields such as optical communication and biological detection. However, high-efficiency phosphors emitting beyond 900 nm remain extremely limited due to non-radiative deactivation. In this study, a 455 nm blue light excitable NIR phosphor that efficiently emits in the wide range of 700-1200 nm (peaking at ~960 nm) was obtained through Cr^{3+}/La^{3+} codoping of Ruddlesden-Popper type $Sr_3Zr_2O_7$ perovskite, whose internal/external quantum efficiencies (%) and thermal stability of luminescence (I_{423}/I_{298}, %) reached ~92.4/57.5 and 73, respectively. Experimental and theoretical analysis found the decisive role of the La^{3+} codopant in Cr^{3+} luminescence: it not only inhibited Cr^{3+} from oxidation but also attracted the Cr^{3+} ions to aggregate around it to form Cr^{3+}-Cr^{3+} pairs for the aforesaid excellent luminescence. Combining the NIR phosphor with a Si-PIN photodetector created a highly effective blue-to-NIR conversion unit, demonstrating application potential of the phosphor for underwater wireless optical communication (UWOC).

Keywords: Near-infrared phosphor, $Sr_3Zr_2O_7$ perovskite, Cr^{3+}-pair luminescence, La^{3+} doping

1 Introduction

With the wide application of near-infrared (NIR) technology in night vision, biological imaging, optical communication and other technical fields, developing high performance NIR light sources has become an urgent task.[1-5] Compared with other NIR light sources, blue-light excited NIR pc-LEDs have drawn wide attention because the technology to fabricate the blue LED chips for excitation has matured and NIR phosphors are relatively easy to synthesize and their excitation/emission can be adjusted through materials design.[6,7] Therefore, in recent years, developing high quality NIR phosphors has become an important research direction in the field of optics.

As one of the most intensely studied NIR activator ions, Cr^{3+} exhibits tunable luminescence by its crystal-field sensitive $3d^3$ energy level. By designing host materials and doping strategies, flexible NIR luminescence in the range of 700-1200 nm can be achieved. Up to now, many Cr^{3+}-activated NIR phosphors have been developed,[8,9] but most of them suffer from unsatisfactory efficiency of blue-light absorption by the parity-forbidden d-d transition of Cr^{3+}, which reduces the matching between the phosphor and commercial blue LED chip. To overcome this, researchers have proposed to enhance orbital mixing and reduce the degree of forbidden by constructing low-symmetry coordination octahedra for Cr^{3+}.[10] Typical examples may include $Ga_{1.6}Sc_{0.4}O_3:Cr^{3+}$ (λ_{em} = 784 nm, λ_{ex} = 442 nm, IQE = 99%),[11] $Ca_{2.7}Na_{0.3}Mg_{0.7}Sb_2Al_{2.3}O_{12}:Cr^{3+}$ (λ_{em} = 760 nm, λ_{ex} = 460 nm, IQE = 90.6%)[12] and $Ca_3Sc_2Si_3O_{12}:Cr^{3+}$ (λ_{em} = 770 nm, λ_{ex} = 460 nm, IQE = 92.3%) phosphors.[13] For luminescence longer than 850 nm, however, high IQE and good thermal stability are

frequently hard to attain since the probability of non-radiative transitions would significantly increase by the reduced energy gap between the lowest-lying excited state (emitting state) and ground state of Cr^{3+},[8] such as in the cases of $LiScP_2O_7:Cr^{3+}$ (λ_{em} = 880 nm/λ_{ex} = 470 nm, IQE = 38%, $I_{423\ K}/I_{298\ K} \approx 20\%$),[14] $NaScSi_2O_6:Cr^{3+}$ (λ_{em} = 845 nm/λ_{ex} = 460 nm, IQE = 64.4%, $I_{423\ K}/I_{298\ K}$ = 75%)[15] and $LiInGe_2O_6:Cr^{3+}$ (λ_{em} = 880 nm/λ_{ex} = 460 nm, IQE = 81.2%, $I_{423\ K}/I_{298\ K} \approx 25\%$).[16] This restricts application in areas like biological detection and optical communication, where NIR lights of longer wavelengths are preferred. Therefore, the development of blue-light excitable NIR phosphors of high efficiency, long emitting wavelength and high thermal stability has significant practical importance.

The novel emission features of Cr^{3+}-Cr^{3+} pairs are drawing wide attention during recent years,[17-22] and the study of which can be dated back to 1961 by Gill et al.[23] In 2024, Wang et al.[24] successfully achieved 913 nm emission of Cr^{3+} pairs with high efficiency (IQE/EQE = 83.9%/35.7%) and good thermal stability ($I_{423\ K}/I_{298\ K}$ = 75.8%) through high concentration Cr^{3+} doping of $Mg_{0.8}Zn_{0.2}Ga_2O_4$ spinel. Despite this success, over-doping of Cr^{3+} activators inevitably induces concentration quenching, thereby reducing the overall intensity of luminescence. Regarding this issue, You et al.[25] designed and synthesized a $BaO(Al_2O_3)_4(ZnAl_2O_4):xCr^{3+}$ phosphor (BAZO:xCr^{3+}, λ_{em} = 750 nm, λ_{ex} = 460 nm, x = 0.06-0.3), where the layered crystal structure effectively alleviated the concentration quenching problem and allowed for high concentration Cr^{3+} doping (x = 0.28). The Ruddlesden-Popper (R-P) type perovskite compounds of $(AO)(ABO_3)_n$ general formula not only have a layered crystal structure but also provide

a [BO_6] octahedral site suitable for Cr^{3+} to occupy, which make them valuable hosts for Cr^{3+} luminescence. In this study, $Sr_3Zr_2O_7$ (SZO), which belongs to the above R-P family, was selected for the first time as the host lattice for Cr^{3+}. By allowing Cr^{3+} to occupy the large-sized and highly distorted [ZrO_6] octahedral sites, we successfully developed in this work a series of blue-light excitable high-performance $Sr_3Zr_2O_7:Cr^{3+},La^{3+}$ (SZCL) NIR phosphors. Theoretical and experimental analyses revealed that the La^{3+} co-dopant may effectively inhibit Cr^{3+} from oxidation, induce the Cr^{3+} ions to redistribute, and promote the creation of Cr^{3+}-Cr^{3+} pairs, with which excellent NIR luminescence was achieved. The SZO:8%Cr,16%La optimal phosphor is not only excitable with 455 nm blue light but also emits at a long wavelength of 960 nm with high quantum efficiency (IQE/EQE = 92.4%/57.5%) and good thermal stability ($I_{423\ K}/I_{298\ K}$ = 73%). The phosphor was also demonstrated to have the potential for application in underwater wireless optical communication (UWOC) technology.

2 Experimental Section

2.1 Materials and Synthesis

The phosphors were synthesized through high temperature solid reaction, using $SrCO_3$ (99.99% pure; Aladdin Bio-Chem. Tech. Co. Ltd, Shanghai, China), ZrO_2 (99.99% pure; Aladdin), La_2O_3 (99.5% pure; Huizhou Ruier Rare-Chem. Co. Ltd, Huizhou, China), and Cr_2O_3 (99.99% pure; Aladdin) as raw materials. The La_2O_3 was dried at 200 ℃ for 2 h before use. The reactants were weighed according to the formulae of $Sr_3Zr_2O_7$, $Sr_3Zr_{1.97}O_7$:0.03Cr, $Sr_{3-x}Zr_{2-x}O_7$:*x*Cr,*x*La (*x* = 0.01-0.1) and $Sr_{3-y}Zr_{1.92}O_7$:0.08Cr,*y*La (*y* = 0-0.2), respectively, and then thoroughly mixed via grounding

with a mortar and pestle for 40 min. The reactant mixture was then transferred into a corundum crucible for solid reaction at 1500 ºC for 6 h in air, with heating rates of 5 ºC /min up to 400 ºC and then 8 ºC /min up to 1500 ºC. All the samples containing Cr ions were subjected to a reduction treatment in a 20 vol% H_2/80 vol% Ar gas mixture (flow rate: 150 mL min^{-1}), where the heating rates are the same as above and the holding time is 2 h. To make a fluorescent film, 0.05 g of the SZO:8%Cr,16%La phosphor was mixed with 0.4g PDMS (Polydimethylsiloxane) glue, followed by spin casting and baking at 60 ºC for 3 h.

2.2 Characterization

X-ray diffractometry (XRD) was performed with a Model SmartLab instrument (Rigaku, Japan) operating at 40 kV/200 mA, using nickel-filtered Cu-Kα radiation as the X-ray source (λ = 0.15406 nm). The XRD data for phase identification were collected over the 2θ range of 20-70° via continuous scan at 10° 2θ/min and those for Rietveld structure refinement were acquired for 2θ = 10-110° via step scan, using a step size of 0.02° and a counting time of 2 s per step. Structure refinement was conducted with the TOPAS version 4.2 software suite. Morphology and elemental distribution were analyzed via field-emission scanning electron microscopy (JSM-7800F, JEOL, Japan; X-max20, OXFORD, UK). Diffuse reflectance spectroscopy (DRS) was performed with a UV-vis spectrophotometer (Model UV-3600 Plus, Shimadzu, Japan) equipped with a 150 mm diameter integrating sphere. Room temperature photoluminescence was analyzed with a Model Fluorolog-3 spectrophotometer (HORIBA, Japan) and all the measurements were carried out with a scan speed of 200

nm min^{-1} and slit widths of 10 nm for excitation/emission. Temperature-dependent photoluminescence and quantum efficiency were measured by a Model FLS1000 fluorospectrometer equipped with an integrating sphere (150 mm in diameter) and a TAP-02 temperature controller (Edinburgh Instruments Ltd., UK). Fluorescence decay was analyzed with a DeltaFlex modular fluorescence lifetime system (HORIBA, Japan), using NanoLED-455 (λ = 450 nm, 1.4 ns pulse duration) as the excitation source. X-ray photoelectron spectroscopy (XPS) was performed with a Model Axis Supra instrument (Kratos Analytical Ltd., UK). Electron paramagnetic resonance (EPR) analysis was conducted at the X-band frequency (9.85 GHz) on a Model Bruker Emxplus instrument (Karlsruhe, Germany).

2.3 Computational Methodology

All the first-principles calculations were carried out using the Castep tool in Materials studio 2020 software, and the details of which can be found in the Supporting Information file.

2.4 Experimental setup of the underwater wireless optical communication (UWOC) system

The signal light source is a blue light laser (450 nm, Laserland, China). Si-PIN (Model S1223-01, Hamamatsu, Japan) was used as photodetector. Electrical signal acquisition was accomplished with an oscilloscope (B2902B, Keysight, USA). A long-pass filter membrane (T80LGM, Anford, China) was employed to block the visible light. Its optical transmission is <2%, ~40% and ~90% in the 400-700 nm, 700-800 nm and 800-1600 nm (near infrared) spectral regions, respectively. A water-filled glass tank of

10 cm × 10 cm × 15 cm was used as the water environment along the signal transmission path.

3 Results and Discussion

3.1 Structure and Luminescence Properties of SZCL

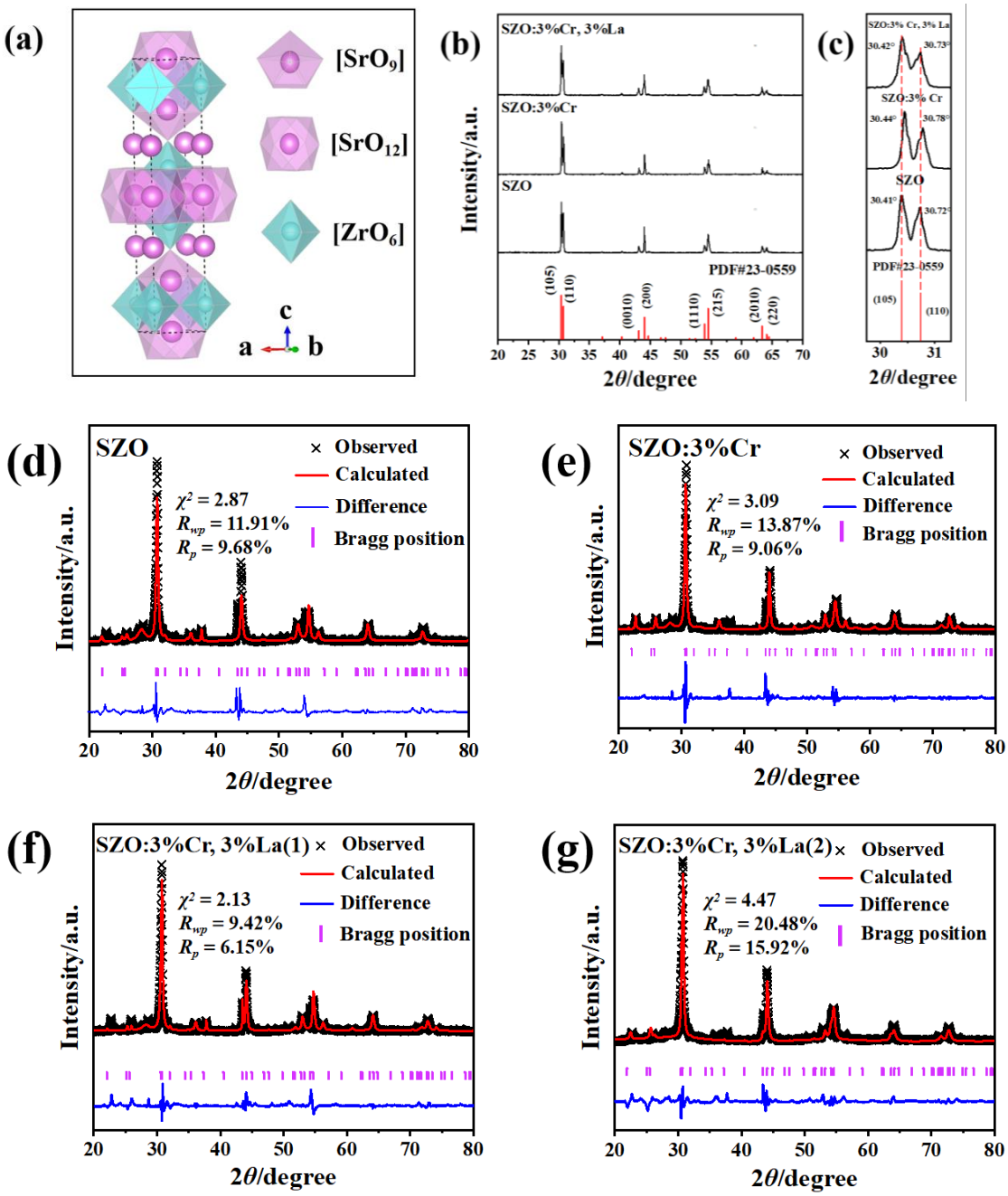

Fig. 1. (a) Schematic crystal structure of SZO; (b) XRD patterns of the SZO, SZO:3%Cr and SZO:3%La,3%Cr powders; (c) enlarged view of the 29.5°-31.5° region of the XRD patterns; Rietveld refinement of the XRD patterns for SZO (d), SZO:3%Cr (e), SZO:3%Cr,3%La(1) (f) and SZO:3%Cr,3%La(2) (g).

$Sr_3Zr_2O_7$ (SZO) crystallizes in the tetragonal system (space group: *I*4/*mmm*) and is featured by a typical R-P type perovskite structure, where the $[SrZrO_3]_2$ double perovskite layer and [SrO] rock-salt layer alternatively stacks along the *c* axis. In such a structure, Zr^{4+} ions exclusively form $[ZrO_6]$ octahedra whereas Sr^{2+} ions form $[SrO_9]$ and $[SrO_{12}]$ polyhedrons,[26] as illustrated in Fig. 1a. It is generally accepted that a dopant ion prefers to replace the host ion of a similar ionic radius. Thus, when Cr^{3+} (0.61 Å for CN= 6, CN: coordination number) was introduced into SZO, it tends to replace Zr^{4+} (0.72 Å for CN = 6) to reside in octahedron. Since the valence mismatch between Cr^{3+} and Zr^{4+} may induce the oxidation of Cr^{3+},[27] La^{3+} was co-doped for charge compensation given its similar radius to Sr^{2+} (1.36 Å for La^{3+} and 1.44 Å for Sr^{2+}, CN = 12). We first synthesized the three samples of SZO, $Sr_3Zr_{1.97}O_7$:0.03Cr (SZO:3%Cr) and $Sr_{2.97}Zr_{1.97}O_7$:0.03Cr,0.03La (SZO:3%Cr,3%La) for comparative studies, whose XRD patterns are shown in Fig. 1b. It is seen that all the samples exhibited diffraction profiles essentially identical to that of the SZO standard (PDF No.23-0559). Close observation (Fig. 1c) found that the (105) and (110) peaks of SZO:3%Cr and SZO:3%Cr,3%La slightly shifted to higher angles, indicating some extent of lattice contraction.

Rietveld refinement of XRD pattern was conducted for the three samples to derive structure details, and the results are shown Fig. 1d-g and Tables S1, S2. From the structure of SZO (Fig. 1a) and ionic size, it is considered that only the $[ZrO_6]$ site is suitable for Cr^{3+} to occupy. For La^{3+}, however, the two sites of $[SrO_9]$ and $[SrO_{12}]$ are available. Therefore, La^{3+} was separately set at the two sites of $[SrO_9]$ (Fig. 1f, La(1))

and [SrO_{12}] (Fig. 1g, La(2)) for the refinement of SZO: 3%Cr,3%La. From the better *R* and χ^2 factor values shown in the Fig. 1f, it can be concluded that La^{3+} inclines to occupy the [SrO_9] site. This is likely because the loose interlayer structure allows for greater local distortion. Table S1 lists the detailed lattice parameters, atomic positions, atomic occupancy, and atomic displacement parameters of the three samples. It can be found that, for either SZO:3%Cr or SZO:3%Cr,3%La, the lattice parameters decreased relative to those of SZO, which is consistent with the higher-angle shifting of diffraction peaks (Fig. 1c). According to the refinement results, Cr^{3+} and La^{3+} preferentially occupy the Zr^{4+} and Sr^{2+} sites with an occupancy of 3%, respectively. Table S2 shows the (Zr,Cr)-O bond lengths, from which the Zr-O bonds in SZO were assayed to have an average length (d_{av}) of ~2.1634 Å. Besides, the [ZrO_6] octahedron was calculated to have a distortion index (Di) of ~0.0632,[28] which is a relatively high value.[10] Therefore, when Cr^{3+} occupies [ZrO_6] octahedron in SZO, a high blue light absorption efficiency may be achieved.

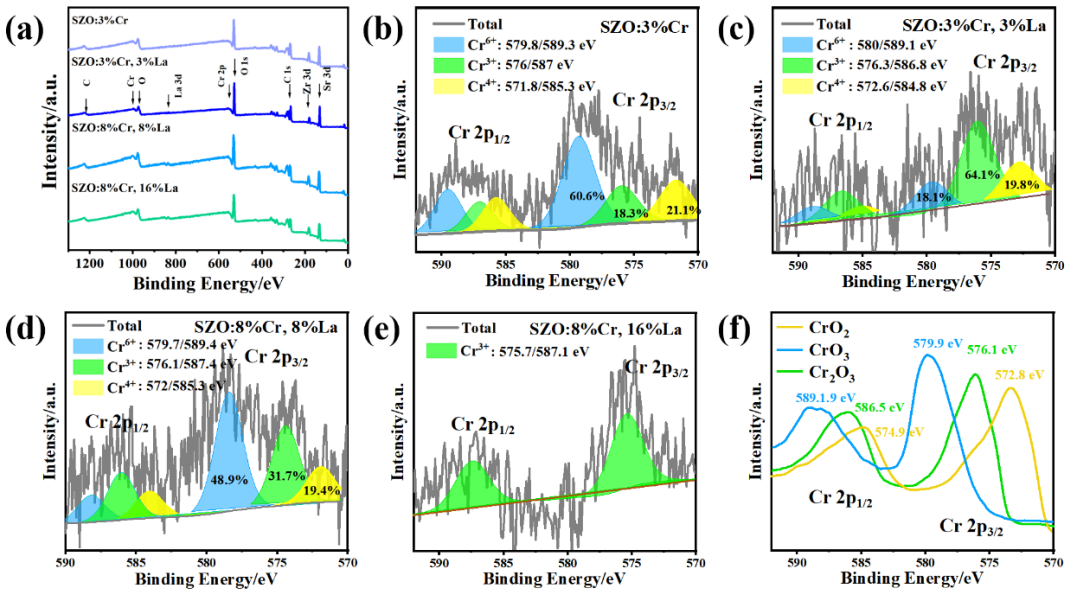

Fig. 2. (a) XPS survey spectra of the SZO:3%Cr, SZO:3%La,3%Cr, SZO:8%La,8%Cr and SZO:8%La,16%Cr samples; (b-e) high resolution XPS spectra for the Cr $2p_{3/2}$ and Cr $2p_{1/2}$ core levels; (f) high resolution XPS spectra of the Cr_2O_3, CrO_2 and CrO_3 reference standards.

After Cr^{3+} doping to form SZO:3%Cr, the d_{av} of (Zr,Cr)-O was shortened to 2.0629 Å, indicating contracted [(Zr,Cr)O_6] octahedra. When La^{3+} and Cr^{3+} were co-doped into SZO to form SZO:3%Cr,3%La, however, the d_{av} of (Zr,Cr)-O was elongated to 2.0941 Å and at the same time the lattice constants of SZO:3%Cr,3%La became slightly larger than those of SZO:3%Cr (Table S1), implying lattice expansion. This expansion can also be perceived from the enlarged view of the XRD patterns in Fig. 1c, where the diffraction peaks of SZO:3%Cr,3%La shifted to smaller angles relative to those of SZO:3%Cr. Such a lattice expansion is abnormal since La^{3+} is smaller than Sr^{2+}. In view of the significant difference in ionic radii among the different valence states of Cr (r_{Cr}^{3+} = 0.61 Å, r_{Cr}^{4+} = 0.55 Å and r_{Cr}^{6+} = 0.44 Å for CN = 6) and the invariable oxidation states of Sr^{2+}, La^{3+} and Zr^{4+}, the abnormal lattice change was supposed to be due to La^{3+}-induced valence change of Cr. To verify this, comparative XPS analysis was performed for the SZO:3%Cr and SZO:3%Cr,3%La samples, and the results are shown in Fig. 2. The survey spectra (Fig. 2a) clearly showed the presence of the constituent elements as well as ubiquitous carbon. Fig. 2b and c shows the high resolution XPS spectra of the 2p core level of Cr in SZO:3%Cr and SZO:3%Cr,3%La, where two asymmetric peaks were well resolved. Each of the peaks can be deconvoluted into three sub-peaks via Gaussian fitting, with those at ~572/585 eV (in yellow), ~576/587 eV (in green) and ~580/589 eV (in blue) well assignable to Cr^{4+}, Cr^{3+} and Cr^{6+}, respectively, according to the high-resolution XPS results reported by Wang et al.[29] It is also seen that these peaks well conform to those of the CrO_2, Cr_2O_3 and CrO_3 reference standards (Fig. 2f), respectively, further confirming the coexistence of Cr^{4+}, Cr^{3+} and Cr^{6+} ions in

either of the samples. From the integral areas of the sub-peaks, the portions of Cr^{4+}, Cr^{3+} and Cr^{6+} were estimated to be ~21.1%, 18.3% and 60.6% for SZO:3%Cr, respectively. Although the SZO:3%Cr sample has been treated in a reducing atmosphere, the low concentration of Cr^{3+} indicates that severe oxidation has occurred. This suggests that hydrogen reduction alone is insufficient to stabilize Cr^{3+} in the SZO lattice. In SZO:3%Cr,3%La, however, the proportion of Cr^{3+} significantly increased to 64.1% while those of Cr^{6+} and Cr^{4+} decreased to 18.1% and 19.8%, respectively. Such results thus clearly indicate that doping La^{3+} at the Sr^{2+} site is an effective strategy to stabilize the valence state of Cr^{3+} through charge compensation. The valence change also proves that the abnormal lattice expansion of SZO:3%Cr,3%La was caused by the increased content of larger Cr^{3+} ions.

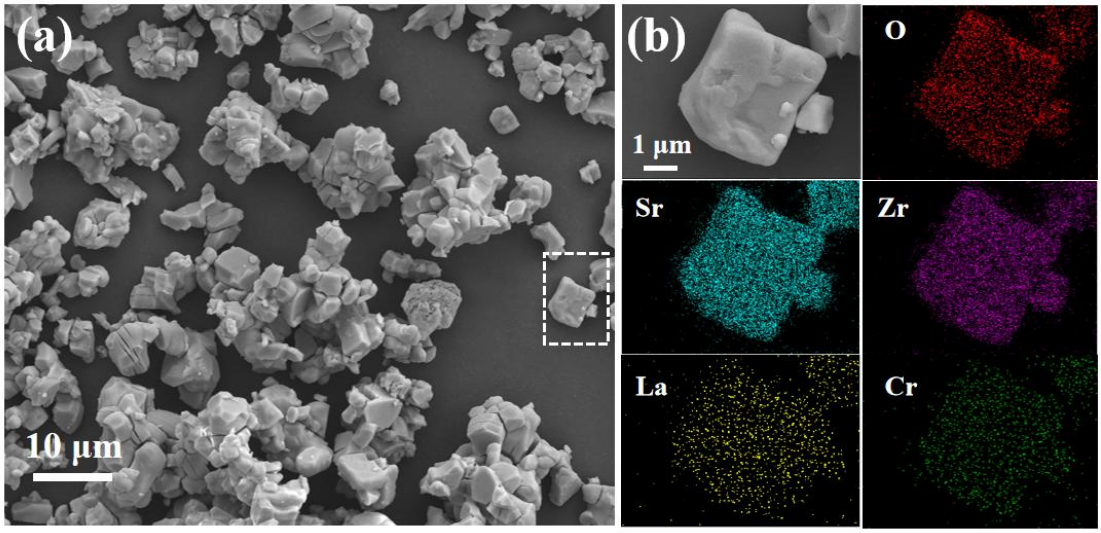

Fig. 3. FE-SEM morphology (a) and EDS elemental mapping (b) for SZO:3%Cr,3%La.

FE-SEM observation (Fig. 3a) found that the SZO:3%Cr,3%La sample contains clusters of micro-sized primary particles, where the tending to be cuboidal morphology may correspond to the tetragonal crystal structure of the material. Elemental mapping

via EDS (Fig. 3b) indicated that the constituent elements are evenly distributed within the particles, confirming the formation of solid solution.

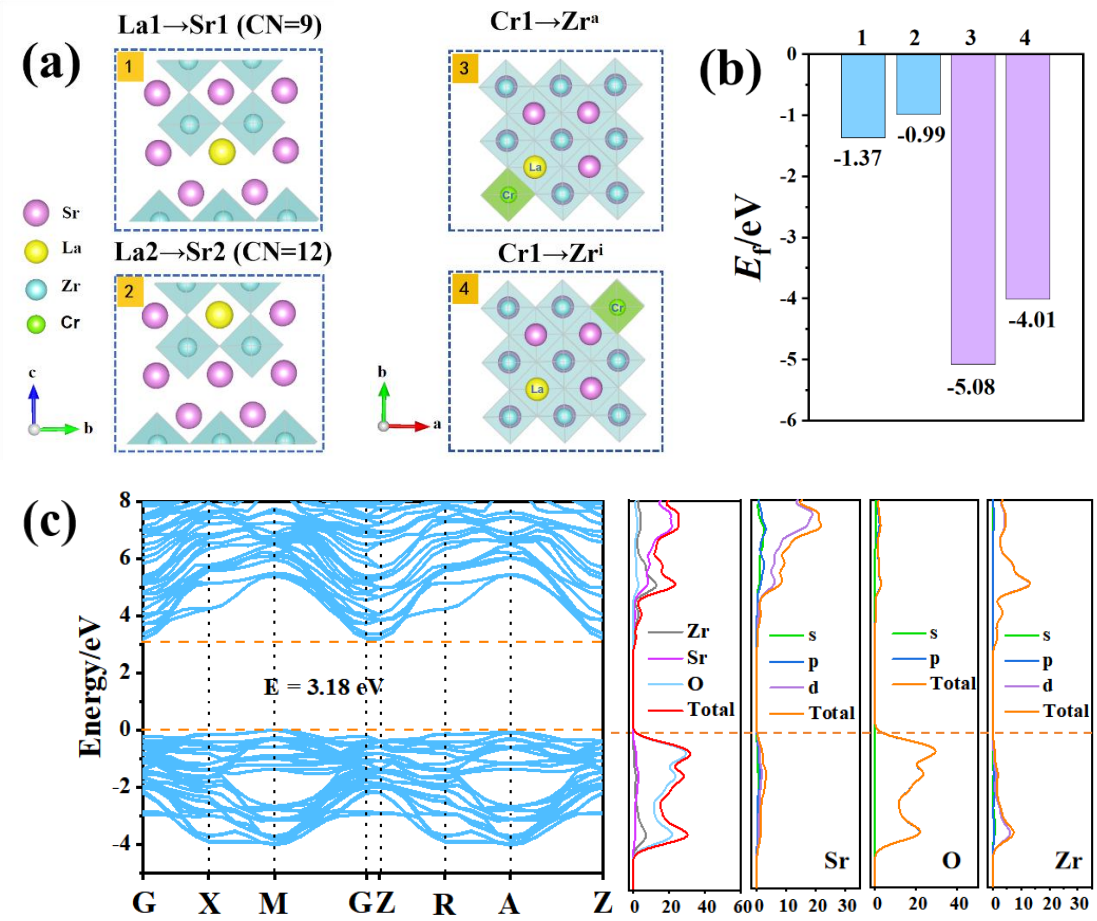

Fig. 4. (a) Schematic of Models 1-4 (substitution model); (b) The formation energy (E_f) for Models 1-4; (c) Calculated band structure, total DOS, and partial density of states (PDOS) of the constituent elements for SZO.

Density functional theory (DFT) was used to evaluate the energetics of La^{3+} incorporation into SZO:Cr. To further confirm lattice occupancy, computation was conducted by assuming that La^{3+} occupies [SrO_9] (Sr1, Model 1; Fig. 4a) and [SrO_{12}] (Sr2, Model 2; Fig. 4a) sites, respectively. Detailed calculation process can be found in the Supporting Information file. From the results shown in Fig. 4b, it can be concluded that, conforming to the finding of Rietveld refinement, La^{3+} indeed prefers [SrO_9] since the computed formation energy (E_f) is lower. With this site preference, the spatial

correlation between La^{3+} and Cr^{3+} was examined, which is the key to understand the mutual interaction of these two types of dopant ions.[30] To determine the preferred relative position, a Cr^{3+} ion was placed at either a Zr site adjacent to La (Zr^a, Model 3; Fig. 4a) or a Zr site distant from La (Zr^i, Model 4; Fig. 4a). Comparison of the E_f for these two configurations (Fig. 4b) revealed a clear energetic preference for the former case (Zr^a site). This indicates that La^{3+} and Cr^{3+} tend to be neighbors in the SZO lattice, which is complying with the case revealed for the $SrTiO_3$:La,Cr analogous system.[31] Such a scenario could be favored by the ease of local charge compensation, since replacing Sr^{2+} with La^{3+} and replacing Zr^{4+} with Cr^{3+} bring about positive and negative charges, respectively.

DFT calculation showed that the SZO host has an indirect bandgap of ~3.18 eV, with the conduction band (CB) and valence band (VB) being primarily composed of Zr 4d and O 2p orbitals, respectively (Fig. 4c). In the band structure of SZO:3%Cr,3%La, the d-orbitals of Cr^{3+} introduce energy states near the Fermi level (Fig. 5a-c). SZO:3%Cr,3%La also shows an anisotropic band structure, since the dispersion from the G to X point, which determines the effective mass of electrons along the [100] direction, spans an energy range of ~1 eV (Fig. 5a) while that from the G to Z point (along [001]) is nearly negligible (Fig. 5a). The effective mass (m^*) of charge carriers is inversely proportional to the second derivative of the *E-k* curve, as follows:[32,33]

$$m^* = \hbar^2 \left(\frac{d^2E}{dk^2}\right)^{-1} \quad (1)$$

The above formula implies a low effective mass and high carrier mobility for a steep

and highly dispersive band and vice versa for a flat band. It can thus be inferred from the results of band analysis that the electron mobility along [100] is much higher than that along [001] in SZO:3%Cr,3%La, and this holds for other in-plane directions such as [110] (G–R). The strongly suppressed electron transport along the [001] direction may effectively isolate the Cr^{3+} ions residing in different layers. This would in turn alleviate concentration quenching even at high doping levels by spatial isolation, as reported for other layer-structured phosphor systems.[24,34,35]

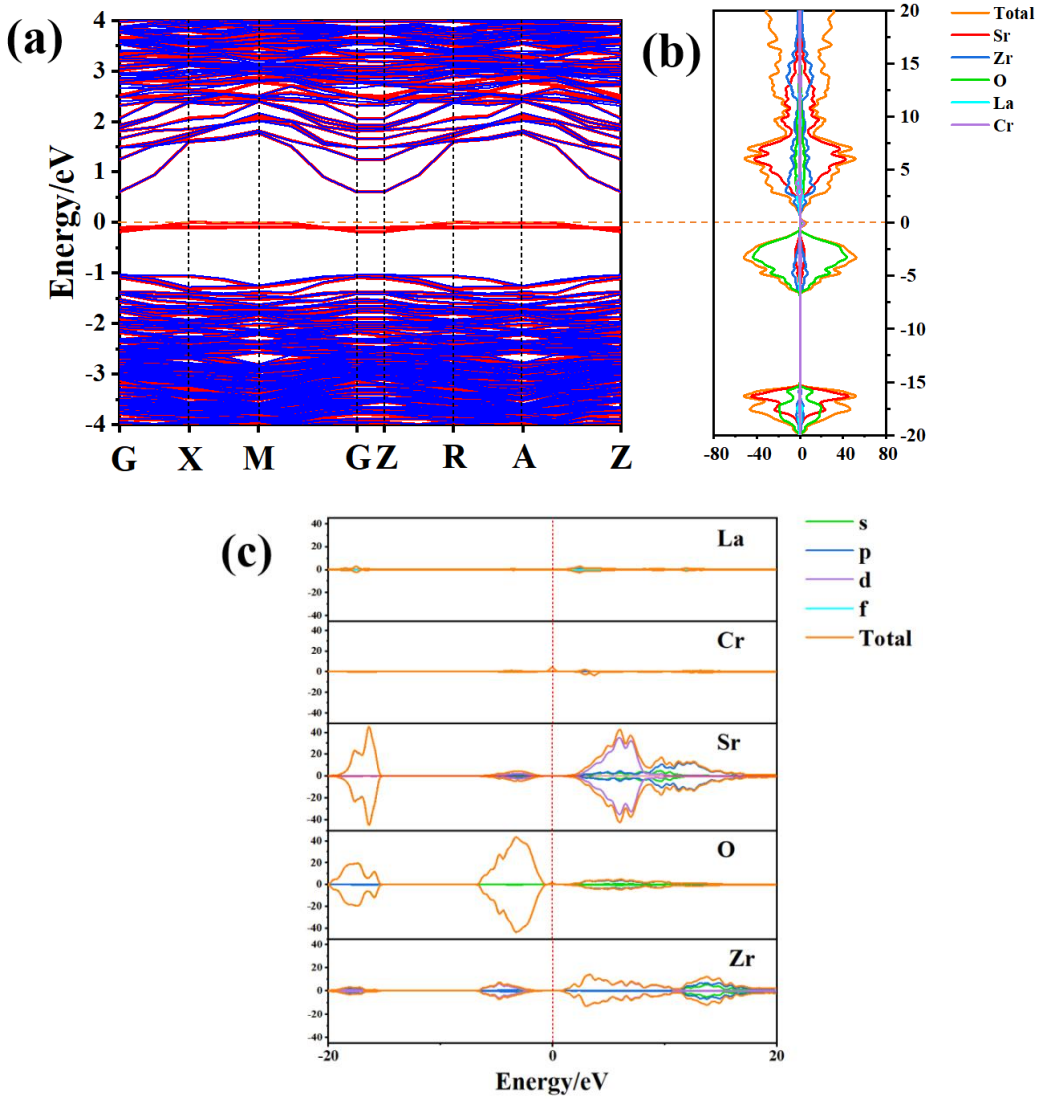

Fig. 5. Calculated band structure (a), total density of states (DOS, b), and partial density of states (PDOS) of the constituent elements (c) for SZO:3%Cr,3%La.

Diffuse reflectance spectroscopy (DRS) of SZO, SZO:3%Cr and SZO:3%Cr,3%La

revealed that SZO mainly absorbs the ultraviolet (UV) light up to ~280 nm (Fig. S1). The optical bandgap of SZO was determined to be ~3.45 eV from the Tauc plot (Fig. S1, the inset),[36-38] which is close to that (3.18 eV) derived via DFT calculation. SZO:3%Cr showed a new absorption band in the 400-750 nm region that is attributable to Cr^{6+} ions.[39] SZO:3%Cr,3%La exhibited two new absorption bands centered at ~461 and 647 nm, which are assignable to the $^4A_2 \rightarrow {}^4T_1\,(^4F)$ and $^4A_2 \rightarrow {}^4T_2\,(^4F)$ transitions of Cr^{3+} ions, respectively. The $^4A_2 \rightarrow {}^4T_1\,(^4P)$ transition of Cr^{3+} overlaps with host absorption, resulting in an intensified composite band at ~275 nm. The results may thus provide optical evidence for the aforesaid effective stabilization of Cr^{3+} ions by La^{3+} incorporation. Particularly, the strong absorption at ~460 nm implies that the SZO:3%Cr,3%La phosphor can be efficiently excited by blue light.

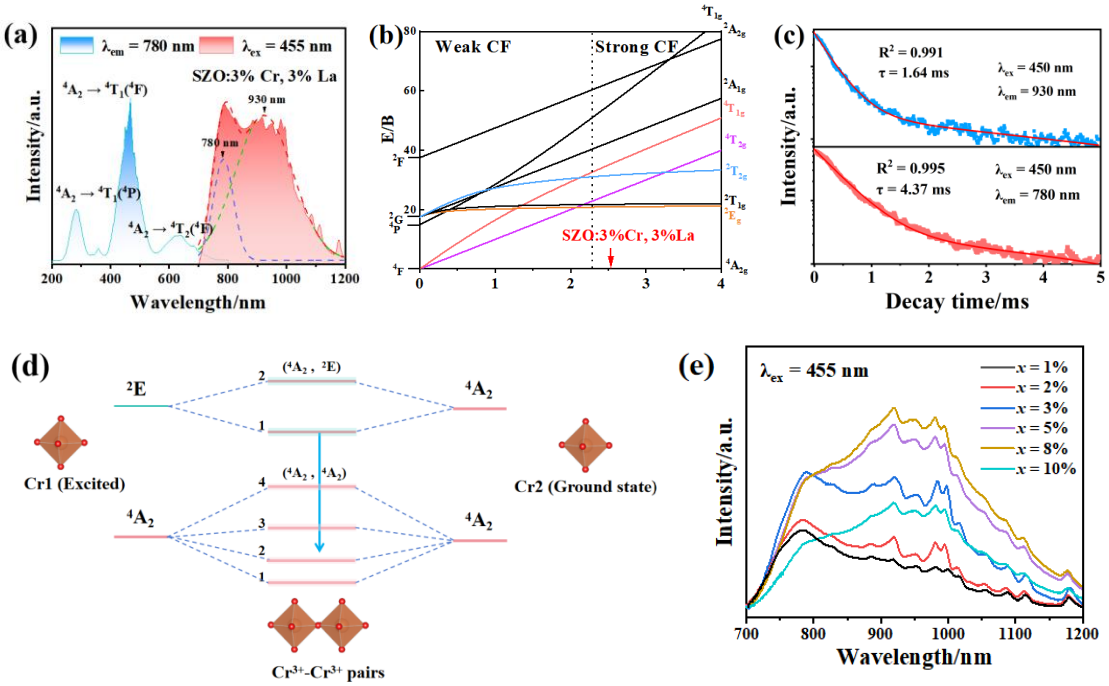

Fig. 6. (a) PL and PLE spectra of the SZO:3%Cr,3%La sample; (b) Tanabe–Sugano energy level diagram for Cr^{3+} under octahedral coordination; (c) Fluorescence decay curves of SZO:3%Cr,3%La; (d) Configurational coordinate diagrams of an isolated Cr^{3+} ion and Cr^{3+}–Cr^{3+} ion pair; (e) PL spectra of SZO:*x*Cr,*x*La (*x* = 1-10%);

Fig. 6a shows the photoluminescence spectra of SZO:3%Cr,3%La. The excitation spectrum (PLE, in light-blue color) contains three bands centered at ~279, 455 (the strongest) and 625 nm, respectively, which are closely matching those found in the DRS spectrum. Under 455 nm excitation, the phosphor outputs a strong emission ranging from ~700 to 1200 nm (PL, in brick red), which can be deconvoluted into two bands centered at ~780 and 930 nm, respectively. The emission behavior of Cr^{3+} is well known to heavily depend on the strength (Dq/B ratio) of its surrounding crystal field, and the values of crystal field splitting energy Dq and Racah parameter B can be derived from the following equations:[40,41]

$$Dq = \frac{E(^4A_2 \rightarrow {}^4T_2)}{10} \tag{2}$$

$$\frac{Dq}{B} = \frac{15(x - 8)}{(x^2 - 10x)} \tag{3}$$

$$x = \frac{E(^4A_2 \rightarrow {}^4T_1) - E(^4A_2 \rightarrow {}^4T_2)}{Dq} \tag{4}$$

For the 780 nm emission, $E(^4A_2 \rightarrow {}^4T_2)$ = 1.968 eV and $E(^4A_2 \rightarrow {}^4T_1)$ = 2.725 eV, thus Dq/B was calculated to be ~2.54, larger than 2.3. This indicates that the Cr^{3+} ions are in a strong octahedral field in SZO, as seen from the Tanabe-Sugano energy level diagram for octahedrally coordinated for Cr^{3+} (Fig. 6b). Such a field strength would give rise to a sharp emission from the $^2E \rightarrow {}^4A_2$ transition of Cr^{3+},[8] which corresponds to the ~780 nm main peak in this work (Fig. 6a). The PL spectrum, however, clearly presents a broad band peaking at ~930 nm. As the PLE acquired by monitoring this emission did not show new spectral features, as compared in Fig. S2, it can be concluded that such an emission did not arise from another separate emitting site or

from Cr in a different valence state but is instead associated with the same Cr^{3+} centers. A number of studies have shown that the Cr^{3+} ions under a high enough concentration tend to form Cr^{3+}-Cr^{3+} pairs by shortened interionic distance, and the ground states of the paired Cr^{3+} ions will couple to form a combined ground state ($^4A_2$, $^4A_2$).[25,42] Under such a circumstance, when one Cr^{3+} ion (Cr1) absorbs energy and becomes excited, energy exchange interaction may occur with the ground state of the other Cr^{3+} ion in the pair (Cr2) to form multi-coupled states such as ($^4A_2$, ^2E) or ($^4A_2$, $^4T_2$) (Fig. 6d). A key spectroscopic signature of such pairs is that their PLE spectrum is virtually indistinguishable from that of a single Cr^{3+} ion, since the initial excitation is localized on a single ion within the pair.[24] Fig. 6c gives the fluorescence decay curves for the 780 and 930 nm emissions of the SZO:3%Cr^{3+},3%La^{3+} phosphor (λ_{ex} = 450 nm), which can be fitted with the following exponential equation:

$$I(t) = I_0 \times A\, exp\,(-t/\tau) \quad (5)$$

where I_0 and $I(t)$ are initial emission intensity and the intensity at decay time t, respectively, A is a pre-exponential constant, and τ is fluorescence lifetime. It is seen from Fig. 6c that the 780 nm emission have a millisecond-level lifetime, characteristic of the spin-forbidden $^2E \rightarrow {}^4A_2$ transition.[6,8] The broad 930 nm emission also has a millisecond-level lifetime, implying that it does not arise from the spin-allowed $^4T_2 \rightarrow {}^4A_2$ transition of Cr^{3+}, which has a microsecond-scale lifetime though typically featured by a wide emission.[43] Noteworthy is that broadband emission of a relatively long lifetime is common for Cr^{3+} pairs. The above results may indicate that the broadband emission near 930 nm originates from Cr^{3+} pairs.

The luminescence properties of Cr^{3+} pairs can be explained by analyzing the coupling effect. When the distance between two Cr^{3+} ions meets the condition for coupling to occur, the spin interaction between them can be described by the following equation:[25,41,44]

$$H_{AB} = -J(S_A S_B) + j(S_A S_B)^2 \quad (6)$$

in which H_{AB} is the Heisenberg Hamiltonian for exchange interaction between two metal ions with spins of S_A and S_B, J is an isotropic bilinear parameter giving the strength of exchange coupling interaction, and j is the exchange parameter for biquadratic exchange. Theoretically, exchange interaction is expected to occur in transition metal ion pairs, including both $3d^n$ and $4f^n$ ions. Given that the contribution of the second term is negligible, the energy eigenvalue $E(S)$ of H_{AB} can be determined by the following equation:[25,41,44]

$$E(S) = -J[S(S+1) - S_A(S_A+1) - S_B(S_B+1)] \quad (7)$$

where S represents the total spin, taking all integer values between the sum ($S_A + S_B$) and the difference $|S_A - S_B|$ of the spin values S_A and S_B of the two ions. For transition metal ion Cr^{3+} (ground state: $^4A_2$, spin $S = 3/2$), the coupling energy levels ($^4A_2$, $^4A_2$) of the two ions' ground states yield four possible spin values of $S = 0, 1, 2, 3$. When one of the Cr^{3+} ions is in the ^2E excited state (spin $S = 1/2$) and the other remains in the ground state, the total spin of the pair's excited state energy level is $S = 1, 2$ (Fig. 6d). Therefore, when two Cr^{3+} ions couple together, the excited and ground state energy levels of the pair will no longer separate from each other but will instead be composed of a series of new levels with small energy differences. When excited, the electrons will

undergo transitions between these densely distributed energy levels, thereby generating a continuous emission band covering a wide energy range. This explains why the 930 nm emission appeared as a broadband in this work.

As pair formation is strongly dependent on the concentration of Cr^{3+}, a series of phase-pure SZO:*x*Cr,*x*La samples (x = 1%-10%; Fig. S3) were synthesized with equimolar of Cr^{3+} and La^{3+} for investigation. PL analysis (λ_{ex} = 455 nm, Fig. 6e) showed that the intensity of Cr^{3+} emission increases with increasing x up to 8%, together with a gradual shifting of the main emission from 780 to 960 nm. This indicates that a suitably high Cr^{3+} content may not only provide more luminescent centers but also dramatically increase the number of Cr^{3+} pairs. Noteworthy is that the emission from Cr^{3+} pairs appeared at a Cr^{3+} concentration (x = 2%, Fig. 5e) well below the onset (x = 8%) of concentration quenching. Generally, when Cr^{3+} ions are randomly distributed in the host, a doping level close to that for quenching concentration to occur is required to meet the distance condition for Cr^{3+} pair formation.[19-22] Therefore, the early emergence of Cr^{3+} pair emission in the SZO:*x*Cr,*x*La phosphors is highly unusual.

3.2 Luminescence optimization

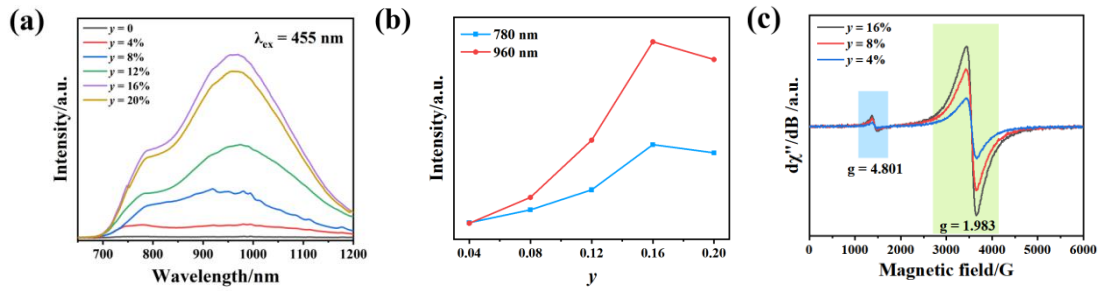

Fig. 7. (a) PL spectra of SZO:8%Cr,*y*La; (b) Emission intensities at 780 and 960 nm as a function of y for SZO:8%Cr,*y*La; (c) EPR spectra of the SZO:8%Cr,*y*%La samples (y = 4%, 8% and 16%).

Since La^{3+} and Cr^{3+} tend to be neighbors, as revealed via DFT calculation (Fig. 4a

and b), we speculated that La^{3+} doping disrupted the random distribution of Cr^{3+} and thus promoted the early formation of Cr^{3+} pairs. To verify this, a series of phase-pure SZO:8%Cr,*y*La (*y* = 0-20%) phosphors were prepared under the fixed optimal Cr^{3+} content of 8%, whose XRD patterns are shown in Fig. S4. PL analysis (Fig. 7a) revealed the dramatic influence of La^{3+} content on Cr^{3+} luminescence. The *y* = 0 sample did not exhibit detectable emission, while La^{3+} doping produced two bands corresponding to $^2E \rightarrow {}^4A_2$ transition of Cr^{3+} and Cr^{3+} pairs at ~780 and 960 nm, respectively. Furthermore, both the emissions gradually gained intensity up to *y* = 16%. When the concentration of isolated Cr^{3+} and Cr^{3+} pair increased further (*y* = 20%), concentration quenching of luminescence occurred, as seen from the luminescence intensity drop in Fig. 7a. This further confirms that La^{3+} doping may effectively inhibit Cr^{3+} oxidation and the effect of inhibition is dependent on La^{3+} content. While the luminescence remained weak up to 8% of La^{3+} (equimolar with Cr), significant intensity enhancement was observed under excessive La^{3+} doping (*y* > 8%). This suggests that super-stoichiometric La^{3+} is required for better suppression of Cr^{3+} oxidation, which was confirmed by the results of XPS analysis shown in Fig. 2d and e. It is seen there that Cr^{3+} comprises only 31.7% of the total Cr species in the SZO:8%Cr,8%La sample whereas nearly all the Cr ions are in the 3+ valence state in SZO:8%Cr,16%La. We also found that the SZO:8%Cr (*y* = 0) and SZO:8%Cr,16%La (*y* = 16%) samples appear brownish and greenish under natural light (Fig. S5), respectively, implying that the dominant Cr species are Cr^{6+} in the former and Cr^{3+} in the latter according to the report of Zhou et al.[45] This further confirms that La^{3+} doping inhibits Cr^{3+}oxidation. It should

be noted that excessive doping of La^{3+} may produce unbalanced point defects such as oxygen interstitials. To determine whether the luminescence enhancement is related to such defects, Al^{3+} ion, whose radius (0.53 Å under CN = 6) is close to that of Cr^{3+} (0.61 Å, CN = 6), was used to replace Cr to form a $Sr_3Zr_2O_7$:8%Al^{3+},16%La^{3+} reference sample under the same synthesis conditions. XRD and PL analyses indicated that the product is a pure perovskite phase but did not show luminescence under 455 nm excitation (Fig. S6). Such a result thus ruled out the possibility of emission from defect-related energy levels.

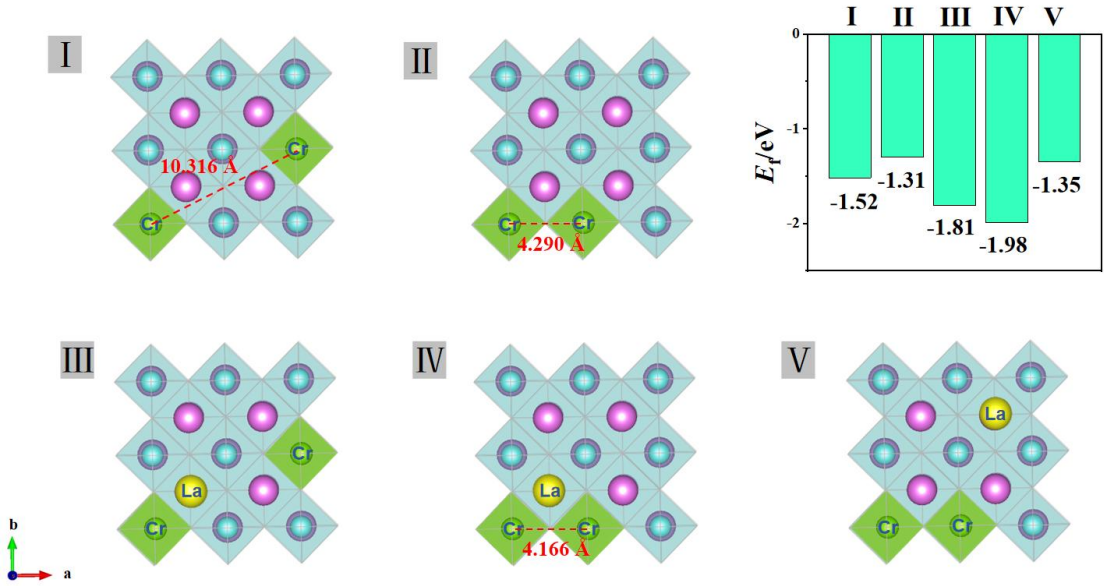

Fig. 8. Schematics for Models I-V, where Models I-II illustrate configurations with two Cr^{3+} ions introduced into the lattice while Models III-V represent three possible configurations for an added La^{3+}, which are based on Models I-II. The E_f of each configuration is displayed in the bar chart.

Although the actual fraction (31.7%) of Cr^{3+} in SZO:8%Cr,8%La is not high, the emission from Cr^{3+} pairs (λ_{em} =960 nm) has become dominant (Fig. 7a). It is also seen from Fig. 7b that the 960 nm emission gains intensity much faster than the 780 nm one with increasing La^{3+} content, further demonstrating that La^{3+} not only suppresses Cr^{3+} oxidation but also promotes the formation of Cr^{3+} pairs. To explore the promotion

mechanism of La^{3+}, we constructed five configurational models to simulate the distribution of Cr^{3+} and La^{3+} and the formation energy (E_f) of Cr^{3+} pairs was evaluated through DFT calculation, as shown in Fig. 8. Models I and II present two Cr^{3+} ions introduced into SZO as separate ones and adjacent ones, which were calculated to have inter-atomic distances of 10.316 and 4.290 Å after structure optimization, respectively. Model I may thus preclude interaction between the ions due to the large separation distance, while Model II may satisfy the distance prerequisite for coupling and allow the formation of a Cr^{3+}-Cr^{3+} pair. The calculated E_f values (Fig. 8), however, showed that Model I is more stable, suggesting that Cr^{3+} pairs are difficult to form in SZO without La^{3+} doping. By introducing a La^{3+} ion into Model I and Model II as a neighbor of Cr^{3+}, the structures shown in Model III and Model IV were obtained, respectively. It is seen from the results of calculation that the E_f of Cr^{3+} pair formation can be significantly reduced from -1.31 to -1.98 eV for Model IV, a value even lower than that of Model III for random distribution of Cr^{3+}. Interestingly, E_f reduction only occurs when Cr^{3+} pair forms around La^{3+} (Model IV). As seen from the result of Model V (Fig. 8), the E_f will significantly increase if Cr^{3+} pair is formed far away from the La^{3+} ion. These results demonstrate that La^{3+} does not uniformly lower the E_f of Cr^{3+} pair globally but instead acts as a center to attract the Cr^{3+} ions to aggregate around it and thus induce Cr^{3+} pairs to form. The driving force behind the phenomenon could be the ease of local charge compensation as mentioned earlier. For Model IV, it is also seen that the separation distance of the two Cr^{3+} ions in a pair formed around La^{3+} is 4.166 Å (Fig. 8), which is smaller than that without La^{3+} doping (Model II, 4.290 Å). This might be because La^{3+} is smaller than Sr^{2+}, which makes the local structure more compact. A

shorter distance will further enhance the coupling of Cr^{3+} ions, thereby making the emission of Cr^{3+} pairs stronger.

Electron paramagnetic resonance (EPR) is used to analyze the local coordination of Cr^{3+} and the quantity of Cr^{3+} pair. Fig. 7c shows the results obtained with SZO:8%Cr,*y*La (*y* = 4%, 8% and 16%). It is seen that all the samples exhibited two main resonance signals, with the g-values of 1.983 and 4.801 attributable to Cr^{3+} pair and isolated Cr^{3+}, respectively.[46] The absence of other signals implies that Cr^{3+} ions do not occupy additional sites in the SZO structure. It is also seen from the figure that the signals of isolated Cr^{3+} and Cr^{3+} pair successively gain intensity with increasing La^{3+} incorporation, manifesting the crucial role La^{3+} in inhibiting Cr^{3+} oxidation and meanwhile promoting Cr^{3+} pair formation. Additionally, the similar linewidths of the g = 1.983 signals indicate that Cr^{3+} pairs occupy the same crystallographic sites in both the samples.[47]

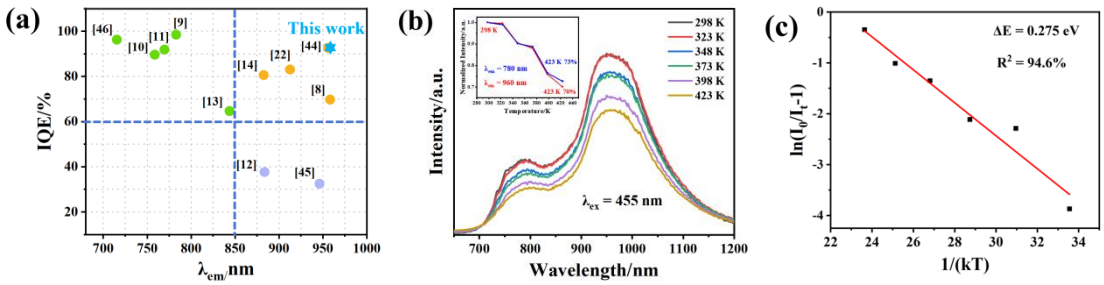

Fig. 9. (a) Performance comparison of the SZO:8%Cr,16%La optimal sample with other reported NIR phosphors, with the reference given as the number in brackets. (b) Temperature dependent emission spectra of SZO:8%Cr,16%La under 455 nm excitation, with the inset showing normalized intensities of the 780 and 960 nm emissions as a function of the measurement temperature, and (c) $\ln(I_0/I_T - 1)$ vs. 1/(kT) relation and linear fitting.

The SZO:8%Cr,16%La optimal phosphor was analyzed to have IQE, EQE and excitation absorption efficiency (AE) of 92.4%, 57.5% and 62.2%, respectively (Fig. S7). As compared in Fig. 9a, the IQE of our phosphor is among the best for various

Cr^{3+}-doped NIR phosphors,[10-16,24,48-50] especially those emitting longer than 850 nm. Such a highly efficient broadband NIR emission (700-1200 nm) is benefiting from the inhibited Cr^{3+} oxidation and promoted Cr^{3+} pair formation by La^{3+} doping. From the temperature-dependent PL spectra (Fig. 9b), it is seen that the luminescence of SZO:8%Cr,16%La was successively weakened by a higher temperature, but the 780 and 960 nm emissions retained ~73 and 70% of their room temperature intensities at 423 K, respectively (Fig. 9b, inset), indicating an excellent thermal stability for phosphors emitting beyond 900 nm.[14-16] Noteworthy is that the different instruments for room temperature (Fluorolog-3) and varying temperature (FLS1000) measurements led to slightly different spectral shapes but no significant difference in the position and relative intensity of the main peaks. The activation energy (ΔE) of thermal quenching can be derived from the equation:[51,52]

$$I_T = \frac{I_0}{1 + Aexp(-\frac{\Delta E}{kT})} \quad (8)$$

Where I_T and I_0 represent the emission intensities at temperature T and room temperature, respectively, A is a preexponential factor and K is the Boltzmann constant. Linear fitting of the $\ln[(I_0/I_T)-1]$ versus $1/T$ transformation of experimental data found ΔE to be ~0.275 eV (Fig. 9c). Generally, a larger ΔE implies that it is harder for electrons to reach the intersection point in the configurational coordinate diagram and thus a better thermal stability of the phosphor. The ΔE value of SZO:8%Cr,16%La is larger than those of Cr^{3+} emission in many other hosts, such as $Mg_{0.8}Zn_{0.2}GaO_4$ (ΔE = 0.265 eV),[24] $NaScSiO_6$ (ΔE = 0.22 eV),[15] $LiInGe_2O_6$ (ΔE = 0.253 eV),[53] and Ga_2GeO_5 (ΔE = 0.254 eV).[54] The good thermal stability makes our phosphor a promising candidate for applications demanding reliable performance in fluctuating thermal

environments.

3.3 Application of the SZO:8%Cr,16%La phosphor in UWOC

UWOC (underwater wireless optical communication) transmits information by converting optical signals into electrical ones using photodiodes. The mainstream incident signal mostly adopts blue light because of its low loss in seawater.[55] At the receiving end, however, blue light signal is not within the optimal response range (700-1000 nm) of the most commonly used Si-PIN photodetector.[56,57] This low response level will seriously affect the strength of the converted electrical signal, thereby influencing the quality of signal transmission. As demonstrated earlier, the SZO:8%Cr,16%La phosphor of this work exhibited excellent performance for blue-to-NIR conversion: it can be efficiently excited by 455 nm blue light and then emit a broad NIR spectrum spanning 700-1200 nm, with a peak wavelength of ~960 nm and high IQE/EQE values of 92.4%/57.5%. More importantly, the PL spectrum of this phosphor strongly overlaps with the optimal response range of the Si-PIN photodetector (700-1000 nm, Fig. 10a).[58] In view of these, we proposed in this work a device (referred to as "coated photodiode" Fig. 10b) for blue light signal conversion, which consists of an NIR fluorescent film (~0.4 mm thick) of the SZO:8%Cr,16%La phosphor, a visible light filter film and a Si-PIN photodiode. The fluorescent film can convert the incident blue light into NIR light to enhance the responsivity of Si-PIN, while the filter can block the original blue light passing through the film, as aforementioned in the Experimental Section, to prevent the two from overlapping and interference. To verify the feasibility of this design, we constructed a laboratory-level prototype UWOC system (Fig. 10c), which consists of a blue light laser (450 nm) as signal source, a water-filled glass tank (10 cm × 10 cm × 15 cm) for water environment, the coated photodiode as signal

receiving end, an oscilloscope for display, and a computer for data processing. In this system, ASCII codes (representing binary numbers) were employed for signal transmission, and an uncoated Si-PIN photodiode of the same type was tested in parallel to serve as a control. The signal was simulated by on/off (1/0) keying of the light source, and the transmitted signal was received by the coated and bare Si-PIN, respectively, and the resulting current waveform was displayed on an oscilloscope and recorded. Fig. 10d shows the waveforms obtained for letters "NEU". It is seen that both the Si-PIN detectors successfully received light signals, but the average intensity of the coated one is approximately 1.58 times that of bare one. The results thus demonstrated that the phosphor of this work may have the potential for application in high performance UWOC systems.

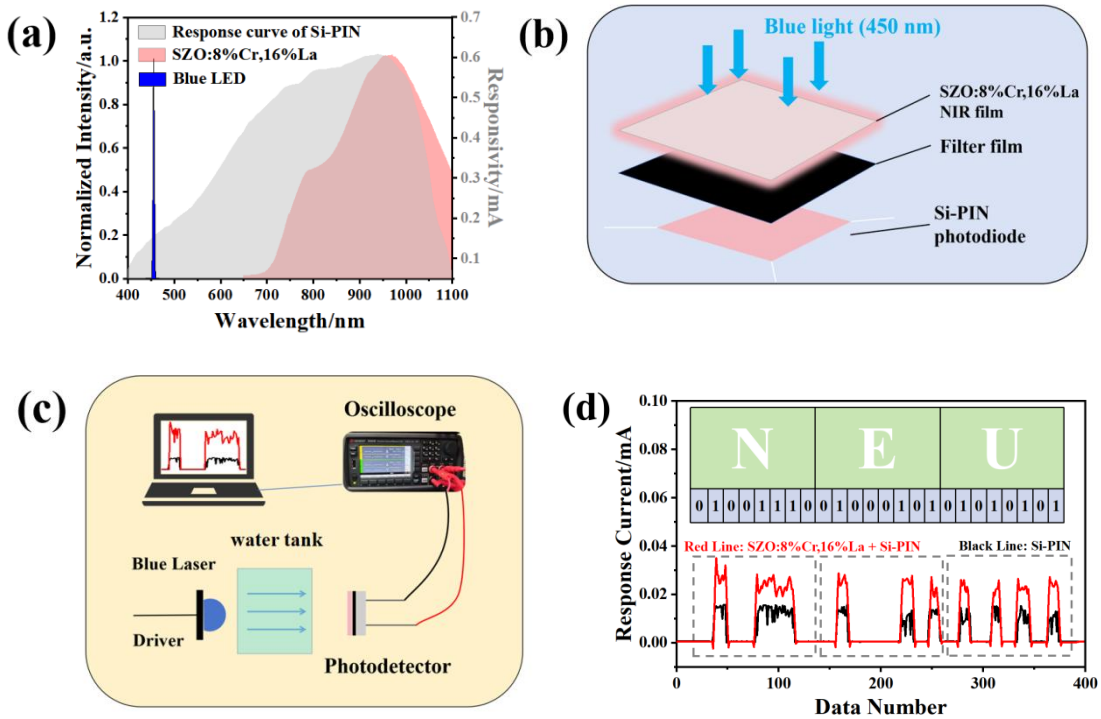

Fig. 10. (a) Comparison of the spectral response of the Si-PIN photodiode with the PL spectra of blue LED source and SZO:8%Cr,16%La phosphor, (b) Schematic illustration of the blue light converter; (c) Schematic illustration of the experimental setup of the UWOC system; (d) Demonstration of transmitting "NEU" ASCII codes in the UWOC system.

Conclusion

This study successfully prepared a series of $Sr_3Zr_2O_7$(SZO):*x*Cr,*y*La (*x* = 0-10%, *y* = 0-20%) NIR phosphors, where the optimal *x* and *y* values are 8% and 16%, respectively. The SZO:8%Cr,16%La optimal phosphor emits NIR light in the wide range of ~700-1200 nm (peak wavelength ~960 nm) under 455 nm blue light excitation, with high internal/external quantum efficiencies (92.4%/57.5%) and good thermal stability (I_{423}/I_{298} ~73%). The La^{3+} co-dopant may inhibit Cr^{3+} from oxidation and meanwhile attract the Cr^{3+} ions to aggregate around it to form pairs, thus playing a decisive role in the luminescence of Cr^{3+}. The phosphor was also demonstrated to have the potential for application in underwater wireless optical communication (UWOC).

Acknowledgements

This work was partially supported by the National Natural Science Foundation of China (Grant No. 52371057)

References

[1] X. Huang, S. Han, W. Huang, X. Liu, Enhancing solar cell efficiency: the search for luminescent materials as spectral converters, *Chem. Soc. Rev.* 2013, 42, 173.

[2] Y. Xie, W. Liu, W. Deng, H. Wu, W. Wang, Y. Si, X. Zhan, C. Gao, X.-K. Chen, H. Wu, J. Peng, Y. Cao, Bright short-wavelength infrared organic light-emitting devices, *Nat. Photonics* 2022, 16, 752-761.

[3] J. Ming, Y. Chen, H. Miao, Y. Fan, S. Wang, Z. Chen, Z. Guo, Z. Guo, L. Qi, X. Wang, B. Yun, P. Pei, H. He, H. Zhang, Y. Tang, D. Zhao, G. K.-L. Wong, J.-C. G. Bünzli, F. Zhang, High-brightness transition metal-sensitized lanthanide near-infrared luminescent nanoparticles, *Nat. Photon.* 2024, 18, 1254.

[4] Y. Wang, Z. Pan, S. Feng, L. Gao, X. Wang, Q. Zhu, and J.-G. Li, Ca^{2+}/Si^{4+} Modification of the (Gd,Lu)AG Garnet for Enhanced Broadband Cr^{3+} Luminescence of High Thermal Stability, *Inorg. Chem.* 2024, 63, 24971-24983.

[5] F. Zhu, Y. Gao, J. Qiu, Sr_2AlTaO_6: Ni^{2+} phosphors with excellent IQE and thermal stability as NIR-II source for night vision, nonvisual detection, and far-field imaging, *Chem. Eng. J.* 2025, 505, 159559.

[6] G. Liu and Z. Xia, Modulation of Thermally Stable Photoluminescence in Cr^{3+}-Based Near-Infrared Phosphors, *J. Phys. Chem. Lett.* 2022, 13, 5001-5008.

[7] H. Zeng, T. Zhou, L. Wang, R.-J. Xie, Two-Site Occupation for Exploring Ultra-Broadband Near-Infrared Phosphor-Double-Perovskite $La_2MgZrO_6:Cr^{3+}$, *Chem. Mater.* 2019, 31, 5245-5253.

[8] F. Zhao, Z. Song, Q. Liu, Advances in Chromium-Activated Phosphors for Near-Infrared Light Sources, *Laser Photonics Rev.* 2022, 16, 2200380.

[9] S. C. Lal, I. N. Jawahar, S. Ganesanpotti, Enhancing the inherent NIR photoluminescence in $SrLaLiTeO_6$ through Cr^{3+}-Yb^{3+} co-substitution for high performance pc-LEDs, *Dalton Trans.*, 2024, 53, 1230–1244.

[10] L. Zhong, Y. Xiang, S. Liu, Z. Chen, Q. Kong, Z. Bai, Y. Ren, F. Xie, C. Jiang, L. Zhou, J.-C. G. Bünzli, M. Wu, Valence and Site Engineering Enable Efficient Broadband Near-Infrared Emission at 960 nm in Cr^{3+}-Activated Forsterite, *Adv. Mater.* 2025, 37, 2508768.

[11] M.-H. Fang, K.-C. Chen, N. Majewska, T. Lesniewski, S. Mahlik, G. Leniec, S. M. Kaczmarek, C.-W. Yang, K.-M. Lu, H.-S. Sheu, R.-S. Liu, Hidden Structural Evolution

and Bond Valence Control in Near-Infrared Phosphors for Light-Emitting Diodes, *ACS Energy Lett.* 2021, 6, 109-114.

[12] Z. Li, G. Zhu, S. Li, W. Xu, Q. Bian, Y. Cong, M. He, X. Luo, S. Xin, B. Dong, High-Performance NIR Emission in Chromium-Doped Garnet Phosphors Enabled by Structure and Excitation Regulation, *Laser Photonics Rev.* 2024, 18, 2300732.

[13] Z. Jia, C. Yuan, Y. Liu, X.-J. Wang, P. Sun, L. Wang, H. Jiang, J. Jiang, Strategies to approach high performance in Cr^{3+}-doped phosphors for high-power NIR-LED light sources, *Light Sci. Appl.* 2020, 9, 86.

[14] L. Yao, Q. Shao, S. Han, C. Liang, J. He, J. Jiang, Enhancing Near-Infrared Photoluminescence Intensity and Spectral Properties in Yb^{3+} Codoped $LiScP_2O_7:Cr^{3+}$, *Chem. Mater.* 2020, 32, 430-2439.

[15] Y. Yan, M. Shang, S. Huang, Y. Wang, Y. Sun, P. Dang, J. Lin, Photoluminescence Properties of $AScSi_2O_6:Cr^{3+}$ (A = Na and Li) Phosphors with High Efficiency and Thermal Stability for Near-Infrared Phosphor-Converted Light-Emitting Diode Light Sources, *ACS Appl. Mater. Interfaces* 2022, 14, 8179-8190.

[16] T. Liu, H. Cai, N. Mao, Z. Song, Q. Liu, Efficient near-infrared pyroxene phosphor $LiInGe_2O_6:Cr^{3+}$ for NIR spectroscopy application, *J. Am. Ceram. Soc.* 2021, 104, 4577-4584.

[17] M. Huang, K. Chen, N. Majewska, M. Kamiński, G. Leniec, E. Mijowska, W. Pang, V. K. Peterson, D.-H. Cherng, K.-M. Lu, S. Mahlik, R.-S. Liu. Spinel-Type Structured Phosphor Near-Infrared-II Emission: Intervalence Charge Transfer and Hetero-Valent Chromium Pairs, *Angew. Chem. Int. Ed.* 2024, 63, e202412815.

[18] Q. Pang, Y. Wang, L. Yan, G. Zhu, S. Xu, J. Zhang, X. Zhang, Y. Cao, B. Chen, Cr^{3+}-Cr^{3+} Ion Pair Induced Fast Energy Migration in Cr^{3+} Doped Na-β-Al_2O_3 Ultra-Wide Near-Infrared Phosphors for NIR Spectroscopy Application, *Laser Photonics Rev.* 2024, 18, 2301039.

[19] X. Chen, X. Huang, Highly Efficient and Thermally Stable NIR-Emitting Phosphor with Largely Tunable Peak Wavelength and Bandwidth Toward NIR Spectroscopy Applications, *Laser Photonics Rev.* 2025, 19, 2402226.

[20] M. Szymczak, A. Antuzevics, P. Rodionovs, M. Runowski, U. R. R.-Mendoza, D. Szymanski, V. Kinzhybalo, L. Marciniak, Bifunctional Luminescent Thermometer-Manometer Based on Cr^{3+}-Cr^{3+} Pair Emission, *ACS Appl. Mater. Interfaces* 2024, 16, 64976-64987.

[21] S. Liu, J. Du1, Z. Song, C. Ma, Q. Liu, Intervalence charge transfer of Cr^{3+}-Cr^{3+} aggregation for NIR-II luminescence, *Light Sci. Appl.* 2023, 12, 181.

[22] H. Zhu, Y. Li, Y. Xi, C. Xin, C. Zhou, Z. Yang, L. Ruan, Y. Li, Y. Peng, M. S. Molokeev, A. Zolotov, J. Wang, Z. Zhou, M. Xia, Abnormal Lattice Shrinkage, Site Occupation, and Luminescent Properties of Cr^{3+}-Activated β-Al_2O_3 Structure Phosphors, *Laser Photonics Rev.* 2024, 19, 2401089.

[23] J. C. Gill, Spin-Lattice Relaxation of Pairs of Chromium Ions in Ruby, *Nature* 1961, 190, 619.

[24] Ge. Chen, Y. Jin, L. Yuan, B. Wang, J. Huo, H. Suo, H. Wu, Y. Hu, F. Wang, Unlocking Cr^{3+}-Cr^{3+} Coupling in Spinel: Ultrabroadband Near-Infrared Emission beyond 900 nm with High Efficiency and Thermal Stability, *ACS Appl. Mater.*

Interfaces 2024, 16, 30185-30195.

[25] X. Zhang, L. Zhou, H. You, Stable and Highly Efficient Near-Infrared Emission Achieved in Spinel Blocks, *Adv. Mater.* 2025, 37, 2419897.

[26] S. Yoshida, K. Fujita, H. Akamatsu, O. Hernandez, A.S. Gupta, F. G. Brown, H. Padmanabhan, A. S. Gibbs, T. Kuge, R. Tsuji, S. Murai, J. M. Rondinelli, V. Gopalan, K. Tanaka, Ferroelectric $Sr_3Zr_2O_7$: Competition between Hybrid Improper Ferroelectric and Antiferroelectric Mechanisms, *Adv. Funct. Mater.* 2018, 28, 18101856.

[27] Y. Xu, G. Abulipizi, Y. Wang, Y. Fang, Z. Yu, J. Zhou, Z. Li, Near-Infrared Persistent Luminescence of $CaTiO_3$:Cr,Y for Imaging of Bone Implants Using Red-Light Illumination Instead of X-ray, *ACS Appl. Mater. Interfaces.* 2024, 16, 55823-55831.

[28] W. H. Baur, The geometry of polyhedral distortions. Predictive relationships for the phosphate group, *Acta Cryst.* 1974, B30, 1195.

[29] Z. Wang, L. Xi, Y. Yang, Y. Li, X. Han, Y. Zuo, J. Wang, Spin-dependent Transport Properties of CrO_2 Micro Rod, *Nano-Micro Lett.* 2014, 6, 365-371.

[30] M. T. Buscaglia, V. Buscaglia, M. Viviani, P. Nanni, Influence of Foreign Ions on the Crystal Structure of $BaTiO_3$, *J. Eur. Ceram. Soc.,* 2000, 20, 1997-2007.

[31] R.B. Comes, P.V. Sushko, S.M. Heald, R.J. Colby, M.E. Bowden, S.A. Chambers, Band-Gap Reduction and Dopant Interaction in Epitaxial La,Cr Co-doped $SrTiO_3$ Thin Films, *Chem. Mater.* 2014, 26, 7073-7082.

[32] X. Sun, X. Xu, Efficient photocatalytic hydrogen production over La/Rh co-doped Ruddlesden-Popper compound Sr_2TiO_4, *Appl. Catal. B-Environ*. 2017, 210, 149-159.

[33] H. Mizoguchi, P.M. Woodward, Electronic Structure Studies of Main Group Oxides Possessing Edge-Sharing Octahedra: Implications for the Design of Transparent Conducting Oxides, *Chem. Mater.* 2004, 16, 5233-5248.

[34] P. A. M. Berdowski, G. Blasse, Luminescence and energy migration in a two-dimensional system: $NaEuTiO_4$, *J. Lumin.* 1984, 29, 243.

[35] L. Tu, X. Liu, F. Wu, H. Zhang, Excitation energy migration dynamics in upconversion nanomaterials, *Chem. Soc. Rev.* 2015, 44, 1331.

[36] Y. Li, B. Yu, H. Wang, Y. Wang, Structural and optical characteristics of novel rare-earth-free red-emitting $BaSn(PO_4)_2:Mn^{4+}$ phosphor, *J. Mol. Struct.* 2021, 1299, 129839.

[37] L. Fang, L. Zhang, H. Wu, H. Wu, G. Pan, Z. Hao, F. Liu, J. Zhang, Efficient Broadband Near-Infrared $CaMgGe_2O_6:Cr^{3+}$ Phosphor for pc-LED, *Inorg. Chem.* 2022, 61, 8815.

[38] P. K. Varriam and S. Ganesanpotti, Harnessing the Dual-Mode Luminescence of Er/Yb Co-Doped $SrLaLiTeO_6$ Double Perovskite Phosphors for Remarkably Wide Range Temperature Sensing and NIR pc-LEDs, *Laser Photonics Rev.* 2024, 18, 2400245.

[39] X. Sun, Y. Xie, F. Wu, H. Chen, M. Lv, S. Ni, G. Liu, X. Xu, Photocatalytic Hydrogen Production over Chromium Doped Layered Perovskite Sr_2TiO_4, *Inorg. Chem.* 2015, 54, 7445-7453.

[40] Y. Tanabe, S. Sugano, On the Absorption Spectra of Complex Ions II, *J. Phys. Soc. Jpn.* 1954, 9, 766-779.

[41] G.C. Liu, M.S. Molokeev, Z.G. Xia, Structural Rigidity Control toward Cr^{3+}-Based

Broadband Near-Infrared Luminescence with Enhanced Thermal Stability, *Chem. Mater.* 2022, 34, 1376-1384.

[42] E. Song, M. Chen, Z. Chen, Y. Zhou, W. Zhou, H.-T. Sun, X. Yang, J. Gan, S. Ye, Q. Zhang, Mn^{2+}-activated dual-wavelength emitting materials toward wearable optical fibre temperature sensor, *Nat. Commun.* 2022, 13, 2166.

[43] P. Luo, D. Sun, Z. Lyu, M. You, Z. Lu, X. Zhang, L. Zhou, H. You, Achieving tunable ultra-broadband NIR emission originating from the two-site occupation of Cr^{3+} ions in $Mg_3Ga_2SnO_8:Cr^{3+}$, *Inorg. Chem. Front*. 2025, 12, 3663-3671.

[44] A.P. Vink, M.A. de Bruin, S. Roke, P. S. Peijzel, A. Meijerink, Luminescence of Exchange Coupled Pairs of Transition Metal Ions, *J. Electrochem. Soc.* 2001,148, E313-E320.

[45] Y. Zhou, Q. Cao, Y. Han, Z. Qiu, Jilin Zhang, W. Zhou, S. Lian, Achieving a Cr^{6+}-free Cr^{3+}-activated spinel phosphor by a one-step solid-state reaction, *Inorg. Chem. Front.,* 2024, 11, 6127–6134.

[46] V. Singh, R.P.S. Chakradhar, J.L. Rao, H.-Y. Kwak, EPR and photoluminescence properties of combustion-synthesized $ZnAl_2O_4:Cr^{3+}$ phosphors, *J. Mater. Sci.* 2010, 46, 2331-2337.

[47] A. A. Prokhorov, L. F. Chernush, T. N. Melnik, R. Minikayev, A. Mazur, V. Babin, M. Nikl, J. Lancok, A. D. Prokhorov, Optical and magnetic properties of the ground state of Cr^{3+} doping ions in $REM_3(BO_3)_4$ single crystals, *Sci. Rep.* 2019, 9, 12787.

[48] F. Zhu, Y. Gao, J. Qiu, High performance NIR-I to NIR-II emission of a Cr^{3+}-doped $Cs_2NaLuCl_6$ phosphor with an IQE and EQE of up to 92.9% and 60.75%, *Inorg. Chem.*

Front. 2024, 11, 7098-7109.

[49] G.C. Liu, M.S. Molokeev, Z.G. Xia, Structural Rigidity Control toward Cr^{3+}-Based Broadband Near-Infrared Luminescence with Enhanced Thermal Stability, *Chem. Mater.* 2022, 34, 1376−1384.

[50] Y. Xiao, L. Han, Z. Xiao, J. Song, T. Li, J. Liu, T. Liu, D. Huang, W. You, X. Han, X. Sun, X. Ye, Near-Unity and Near-Zero-Thermal-Quenching Luminescent GAGG–Al_2O_3:Cr^{3+} Ceramic via Containerless Solidification and Glass Crystallization Methods for NIR Spectroscopy Application, *Laser Photonics Rev.* 2025, 19, 2500165.

[51] Y. Zhou, C. Li, Y. Wang, Crystal-Field Engineering Control of an Ultraviolet–Visible-Responsive Near-Infrared-Emitting Phosphor and Its Applications in Plant Growth, Night Vision, and NIR Spectroscopy Detection, *Adv. Opt. Mater.* 2022, 10, 2102246.

[52] L. Chen, S. Yu, Gu. Shen, S. Tang, T. Zhang, J.-G. Li, Q. Zhu, Large-scale irrigation of Cr^{3+} into different octahedra of zinc aluminate toward continual broadband near-infrared emission, *Ceram. Int.* 2024, 50, 1956-1969.

[53] X. H. Chen, E. H. Song, Y. Y. Zhou, F. Q. He, J. Q. Yang, Q. Y. Zhang, Distorted octahedral site occupation-induced high-efficiency broadband near-infrared emission in $LiScGe_2O_6$:Cr^{3+} phosphor, *J. Mater. Chem. C* 2021, 9, 13640-13646.

[54] C.-Y. Peng, B. Wang, L.-F. Yuan, K.-G. Hu, G. Chen, H.-Y. Wu, Y.-H. Hu, Y.-H. Jin, Six- and five-coordinated Cr^{3+} in Ga_2GeO_5 invokes tunable broadband near-infrared emission toward night-vision applications, *Rare Met.* 2023, 42, 3787-3796.

[55] S. A. Sullivan, Experimental Study of the Absorption in Distilled Water, Artificial Sea Water, and Heavy Water in the Visible Region of the Spectrum, *J. Opt. Soc. Am.* 1963, 53, 962-968.

[56] P. Buzhan, B. Dolgoshein, L. Filatov, A. Ilyin, V. Kantzerov, V. Kaplin, A. Karakash, F. Kayumov, S. Klemin, E. Popova, S. Smirnov, Silicon photomultiplier and its possible applications, *Nucl. Instrum. Meth. A,* 2003, 504, 48-52.

[57] S.J. Lange, T.O. Buchmann, M. Sebek, M.L. Welsch, E.J.R. Kelleher, N. Kawai, H. Takahashi, K. Katsuyama, P.U. Jepsen, Lightwave-Driven Long-Wavelength Photomultipliers, *Laser Photonics Rev*. 2024, 18, 2300417.

[58] HAMAMATSU, SI-PIN photodiodes datasheet [EB].2023.